

# A Survey for Hydroxyl in the THOR Pilot Region around W43

Andrew J. Walsh<sup>1\*</sup>, Henrik Beuther<sup>2</sup>, Simon Bihl<sup>2</sup>, Katharine G. Johnston<sup>2,3</sup>, Joanne R. Dawson<sup>4,5</sup>, Jürgen Ott<sup>6</sup>, Steven N. Longmore<sup>7</sup>, Q. Nguyễn Luong<sup>8,9</sup>, Ralf S. Klessen<sup>10,11,3</sup>, Sarah Ragan<sup>3</sup>, Naomi McClure-Griffiths<sup>13</sup>, Andreas Brunthaler<sup>14</sup>, James Urquhart<sup>14</sup>, Karl Menten<sup>14</sup>, Frank Bigiel<sup>10</sup> Friedrich Wyrowski<sup>14</sup> and Michael Rugel<sup>2</sup>

<sup>1</sup>International Centre for Radio Astronomy Research, Curtin University, GPO Box U1987, Perth WA 6845, Australia

<sup>2</sup>Max Planck Institute for Astronomy, Königstuhl 17, 69117 Heidelberg, Germany

<sup>3</sup>School of Physics and Astronomy, University of Leeds, Leeds, LS2 9JT, UK

<sup>4</sup>Department of Physics and Astronomy and MQ Research Centre in Astronomy, Astrophysics and Astrophotonics, Macquarie University, NSW 2109, Australia

<sup>5</sup>Australia Telescope National Facility, CSIRO Astronomy and Space Science, PO Box 76, Epping, NSW 1710, Australia

<sup>6</sup>National Radio Astronomy Observatory, P.O. Box O, 1003 Lopezville Road, Socorro, NM 87801, USA

<sup>7</sup>Astrophysics Research Institute, Liverpool John Moores University, 146 Brownlow Hill, Liverpool L3 5RF, UK

<sup>8</sup>National Astronomical Observatory of Japan, Chile Observatory, 2-21-1 Osawa, Mitaka, Tokyo 181-8588, Japan

<sup>9</sup>EACOA Fellow at NAOJ, Japan & KASI, Korea

<sup>10</sup>Universität Heidelberg, Zentrum für Astronomie, Institut für Theoretische Astrophysik, Albert-Ueberle-Str. 2, D-69120 Heidelberg, Germany

<sup>11</sup>Department of Astronomy and Astrophysics, University of California, 1156 High Street, Santa Cruz, CA 95064, USA

<sup>12</sup>Kavli Institute for Particle Astrophysics and Cosmology, Stanford University, SLAC National Accelerator Laboratory, Menlo Park, CA 94025, USA

<sup>13</sup>Research School of Astronomy & Astrophysics, The Australian National University, Canberra ACT 2611, Australia

<sup>14</sup>Max Planck Institut für Radioastronomie, Auf dem Hügel 69, D-53121, Bonn, Germany

15 August 2018

## ABSTRACT

We report on observations of the hydroxyl radical (OH) within The HI, OH Recombination line survey (THOR) pilot region. The region is bounded approximately between Galactic coordinates  $l=29.2$  to  $31.5^\circ$  and  $b=-1.0$  to  $+1.0^\circ$  and includes the high-mass star forming region W43. We identify 103 maser sites, including 72 with 1612 MHz masers, 42 showing masers in either of the main line transitions at 1665 and 1667 MHz and four showing 1720 MHz masers. Most maser sites with either main-line or 1720 MHz emission are associated with star formation, whereas most of the 1612 MHz masers are associated with evolved stars. We find that nearly all of the main-line maser sites are co-spatial with an infrared source, detected by GLIMPSE. We also find diffuse OH emission, as well as OH in absorption towards selected unresolved or partially resolved sites. Extended OH absorption is found towards the well known star forming complex W43 Main.

**Key words:** masers – stars: formation – ISM: molecules

## 1 INTRODUCTION

### 1.1 OH masers in star forming regions

The star formation process in our Galaxy, including how both low- and high-mass stars are formed, is important to study as it determines how we view galaxies and how

stars and planets are created. Decade long efforts have made significant progress, although the full details are yet to be realised. In particular, the formation of high-mass stars is difficult to study as they form in complex cluster environments that are rare. Although the formation of low-mass stars either in clusters or in isolation is more accessible, it is still difficult to define a self-consistent detailed model that accounts for the wide variety of observational phenomena associated with the formation of stars of all

\* E-mail: andrew.walsh@curtin.edu.au

masses (Mac Low & Klessen 2004; McKee & Ostriker 2007; Zinnecker & Yorke 2007).

In essence, our difficulties in understanding the star formation process are largely associated with our limited ability to study catalogued examples, each of which can only tell us about how star formation looks at one specific location. With a large ensemble of star formation examples to study, there is the promise that all the examples can be put together to form a coherent picture. However, the cataloguing process necessarily introduces biases into any ensemble, which must be taken into account. Therefore, we need to study the full population of star forming sites throughout the Galaxy, in order to form a full picture of the star formation process. Such a grand catalogue is difficult to realise and so in recent years an alternate approach has been explored. This approach is to conduct untargetted surveys of the Galaxy, using many different Galactic Plane surveys, each of which focus on a particular aspect relevant to star formation and then complement the data with theoretical models to help us astrophysically interpret the data. The untargetted approach allows the observer to find the full population of objects within their survey, rather than picking out selected targets from another survey, with its own biases. Many different Galactic Plane surveys are required in this approach because each untargetted survey may only observe a select aspect of the star formation process. A classic example of this is the Infrared Astronomical Satellite (IRAS) point source catalog (Beichman et al. 1988), which proved extremely useful in identifying all the bright and red far-infrared sources within the Galaxy (Wood & Churchwell 1989) which are typically associated with high-mass star formation. However, early stages of high-mass star formation take place in infrared-dark clouds (IRDCs – Rathborne, Jackson & Simon 2006) and so were not detected by IRAS. Thus, IRAS could only be used to identify star formation sites that were reasonably well evolved, but still embedded in their natal molecular clouds.

Currently, there are many untargetted Galactic plane surveys that are relevant to star formation. There are continuum surveys from short to long wavelengths including: the near-infrared (eg. 2MASS – Skrutskie et al. 2006, UKIDSS – Lawrence et al. 2007), mid-infrared (eg. MSX – Egan & Price 1996, GLIMPSE – Churchwell et al. 2009; Benjamin et al. 2003, MIPSGAL – Carey et al. 2009), far-infrared and sub-millimetre (IRAS – Beichman et al. 1988, Hi-GAL – Molinari et al. 2010, ATLASGAL – Schuller et al. 2009), millimetre (eg. BGPS – Ginsburg et al. 2013) and centimetre (eg. CORNISH – Purcell et al. 2013, VGPS – Stil et al. 2006, SGPS – Haverkorn et al. 2006, CGPS – Taylor et al. 2003). These continuum surveys allow a wide range of physical conditions to be probed, from ionised gas to hot gas and dust to cold dust. In addition to the continuum surveys, there are also spectral line surveys, which can be used as diagnostics of particular aspects of the star formation process: CO (eg. Dame, Hartmann & Thaddeus 2001; Jackson et al. 2006; Burton et al. 2013), CS (MALT-45 – Jordan et al. 2013), NH<sub>3</sub> (HOPS – Purcell et al. 2013), OH (eg. SPLASH – Dawson et al. 2014) and HI (eg. SGPS – McClure-Griffiths et al. 2005). In addition to the above-mentioned spectral line surveys are spectral line surveys

of strong masers: class I methanol masers (eg. MALT-45 Jordan et al. 2013), water masers (eg. HOPS – Walsh et al. 2012), class II methanol masers (eg. MMB – Green et al. 2009) and OH masers (eg. SPLASH – Dawson et al. 2014). All these surveys can help build a detailed picture of the star formation process whilst minimising inherent biases in sample selection.

## 1.2 OH masers and evolved stars

OH masers are commonly found in the later stages of stellar evolution, particularly during the asymptotic giant branch (AGB) phase and shortly thereafter. The AGB phase occurs for stars with masses 1-8 M<sub>⊙</sub> where the main supply of nuclear fuel (hydrogen) in the core is exhausted. The outer atmosphere is expelled from the surface of the star in a dense stellar wind that expands isotropically at typical velocities of 5-30 km s<sup>-1</sup>, forming an envelope. The expanding circumstellar envelope can harbour masers from SiO, H<sub>2</sub>O and OH, with SiO masers found closest to the star and OH masers found furthest away, which is probably due to the differing excitation temperatures of the masing transitions (Reid & Moran 1981).

OH masers that occur in the circumstellar envelopes are typified by a double-horned profile, where the outer edges, showing the strongest maser emission, are indicative of red-shifted and blue-shifted gas moving behind and in front of the central star, respectively. Thus, the OH maser profile may be used to characterise the kinematics of the circumstellar envelope. This distinctive profile also allows the easy identification of OH masers associated with evolved stars.

Eventually, the star evolves from the AGB stage into a planetary nebula (PN), through a very short-lived ( $\sim 30 - 10^4$  years; Blöcker 1995) post-AGB phase. During this evolution, the masers that originate in the circumstellar envelope are extinguished. The SiO masers turn off first, followed by H<sub>2</sub>O masers, leaving the OH masers to disappear last. Most PNe are observed to be highly asymmetric. It is not entirely understood how the symmetric AGB star and attendant envelope evolve into an asymmetric PN. A possible method is that high velocity bipolar jets are formed during the post-AGB phase that impinge on the nearly-symmetric circumstellar envelope, where small density variations create the asymmetric PN (Sahai & Trauger 1998). Both H<sub>2</sub>O and OH masers are seen to trace such jets in the post-AGB phase (eg. Imai et al. 2002; Zijlstra et al. 2001). These high velocity jets are exceedingly rare, due to their extremely short lifetimes.

Another exceedingly rare class of objects associated with evolved stars are OHPNe (Uscanga et al. 2012). These objects show radio continuum emission associated with a PN, but also show OH maser emission. It is likely that this phase occurs when the PN phase has just started, with the inner part of the circumstellar envelope already ionised, but the outer parts harbouring OH masers.

It is therefore important that we increase the numbers

of known examples of these rare, short-lived phases through maser surveys so that we can study these important phases of stellar evolution.

### 1.3 A Pilot OH Survey for THOR

The work described here is part of The HI, OH, Recombination line survey of the Milky Way (THOR). THOR is a Northern Hemisphere Galactic plane survey that includes continuum emission, as well as spectral lines of HI, radio recombination lines and the ground-state OH transitions. THOR surveys a large fraction of the Northern Galactic plane ( $l = 15^\circ - 67^\circ, |b| \leq 1^\circ$ ), using the Karl G. Jansky Very Large Array, with a spatial resolution of about  $20''$ . Apart from OH lines, THOR also maps HI, continuum in the 1-2 GHz range and multiple radio recombination lines. The work reported in this paper focuses on data from the THOR pilot survey, covering  $l = 29.2 - 31.5^\circ, |b| \leq 1^\circ$  and includes the W43 and W43-South high-mass star formation complexes. HI data (Bihl et al. 2015) and continuum data (Bihl et al. *in preparation*) from the pilot region will be published elsewhere, as will a full survey description (Beuther et al. *in preparation*). The focus of this work is on OH emission and absorption. The OH radical has four ground-state transitions around 1.6-1.7 GHz. All four transitions are known to exhibit strong maser emission, which is easily detectable in a survey such as THOR. SPLASH is a complementary survey to THOR. SPLASH concentrates on emission from the hydroxyl radical (OH) in the Southern Hemisphere, where this work is part of a Northern Hemisphere survey. A detailed introduction on the OH ground-state transitions can be found in the SPLASH pilot paper (Dawson et al. 2014).

### 1.4 A note on maser terminology

In the literature, some confusion exists over terminology used to describe various aspects of maser emission. In particular, the term “maser spot” has multiple definitions. For example, (Walsh et al. 2001) give a definition in terms of methanol masers as: “A methanol maser spectrum typically consists of many peaks. Each peak corresponds to a well-defined position in the sky, referred to as a maser spot. Maser spots are usually seen to cluster on a scale of less than 1 arcsec. These clusters are referred to as maser sites.” However, an alternate definition is provided by Imai et al. (2000), who in turn cite Gwinn (1994) as: “A maser spot is a single velocity component of the maser emission. A maser feature is a group of the maser spots with similar positions (within several hundred microarcseconds) and with successive velocities (with spacings  $0.3-3 \text{ km s}^{-1}$ ). Spots thus reflect somewhat instrumental factors, especially the velocity spacing of each channel.”

The important difference between these definitions is that a maser spot in the first definition is essentially the same as a maser feature in the second definition. But there is no equivalent to the maser spot used by Imai et al. (2000). Whilst different definitions may be common in

fields of research, it appears that both definitions of maser spot are in common usage within the maser community. Furthermore, much work is published where maser spot and maser feature are used interchangeably. Thus there is a strong need to consolidate terminology amongst researchers to avoid future confusion.

The term “maser hot spot” was introduced by Litvak (1971) in response to high spatial resolution observations by Moran et al. (1968), Burke et al. (1970) and Johnston et al. (1971). Moran et al. (1968), for example, observed OH masers in W3 and found “knots of radiation”, corresponding to single peaks in the spectrum, where the “ratio of separation to size is typically 100 to 1.” The sizes of the maser hot spots in these observations were around  $10^{14} \text{ cm}$  ( $\sim 10 \text{ AU}$ ), whereas typical separations were around  $10^{16-17} \text{ cm}$ . The terminology “maser hot spot” by Litvak (1971) was introduced to highlight that the masers originated in small regions of the sky where it was thought a single parcel of gas was responsible for the exceedingly high brightness temperatures that were measured. This terminology was quickly contracted by subsequent authors to “maser spot” and became common usage.

The observations by Gwinn (1994) identified that a maser spot (using the definition of Litvak 1971) may break up into substructures that are found to have slightly (but significant) different positions for each channel in the data that was analysed. Thus, the terminology was changed to highlight that a maser feature corresponds to a physical entity that typically corresponds to a single peak in a spectrum and a maser spot became the name assigned to the substructure evident between single channels of a spectrum and within a single maser feature. However, this new terminology means that a maser spot is governed by instrumental effects (ie. the channel resolution), rather than corresponding to a single parcel of gas at a well defined position that gives rise to a single peak in the spectrum. Thus, the term maser spot loses its meaning in the context of a hot spot.

In this work, we use the term maser spot in keeping with its original definition as a contraction of maser hot spot which constitutes a single peak in the spectrum. Such maser spots are expected to have sizes around  $10^{14} \text{ cm}$  and are occasionally grouped into regions with sizes around  $10^{16-17} \text{ cm}$ , which we call maser sites. However we note that, given our spatial resolution and typical distances to masers, maser spots will be unresolved in our work. Indeed, most maser sites will also remain unresolved in this work. We remind the reader that our definition of “maser spot” is in common usage as either “maser feature” or “maser component” in other work.

## 2 OBSERVATIONS AND DATA REDUCTION

### 2.1 VLA Observations

We mapped a  $2^\circ \times 2^\circ$  field around W43 ( $l = 29.2-31.5^\circ, |b| \leq 1^\circ$ ) during the 2012A semester with the Karl G.

Jansky Very Large Array (VLA) in New Mexico in C-configuration (Project 12A-161). The phase centre of the observations was  $18^{\text{h}}46^{\text{m}}45^{\text{s}}.4, -02^{\circ}16'19''$ . The primary beam at 1667 MHz has a FWHM of  $27'$ . A total of 59 pointings were used to cover the 4 square degree mosaic. With a broad frequency coverage between 1 and 2 GHz, the primary beam sampling is a compromise between sampling density and area coverage. For the Pilot region detailed in this work, we used a mosaicing scheme consisting of a hexagonal grid with  $17.9'$  spacing. This results in excellent data quality with very little variation in sensitivity in the inner survey region. However, for the full survey, we improved the sampling to  $15'$  spacing, using a square grid so that the data are Nyquist sampled at the H $\alpha$  line frequency (1.42 GHz).

Each pointing was observed  $4 \times 2$  minutes, resulting in an overall observation time of 10 hours. The observations were conducted in two blocks each with 5 hours observing time in April 2012. We chose the quasar 3C286 as a flux and bandpass calibrator and the quasar J1822-0938 as a complex gain calibrator, which was observed every 13 minutes. Observing at L-band and using the new WIDAR correlator, we were able to simultaneously observe the H $\alpha$  line, the 4 OH lines (1612, 1665, 1667 and 1720 MHz) and 12 H $\alpha$  radio recombination lines. The continuum, detected in eight spectral windows between 1 and 2 GHz, was observed in full polarisation. The spectral lines were only observed in LL and RR polarisations. However, we only present stokes I information on the OH lines in this work. For the OH lines, we used a bandwidth of 1 MHz with a channel width of 3.906 kHz. This results in a velocity range of about  $180 \text{ km s}^{-1}$  and a channel spacing of  $0.73 \text{ km s}^{-1}$  at 1612 MHz.

We use a synthesised beam of  $20'' \times 20''$ . With this beam, we estimate the absolute positional accuracy is  $\Theta_{\text{BEAM}}/2\text{SNR}$  (Fomalont 1999) where  $\Theta_{\text{BEAM}}$  is the beam size ( $20''$ ) and SNR is the signal to noise ratio. Under typical observing conditions, we conservatively expect the absolute positional accuracy to be no better than 10 per cent of the beam (ie.  $2''$ ). With a typical rms noise level of 19 mJy/beam per  $0.73 \text{ km s}^{-1}$  channel (see Section 3.1 for further details), this means that for any point source stronger than  $5\sigma$ , the absolute accuracy will be  $2''$ . For weaker point sources, the accuracy will be lower and will follow  $\Theta_{\text{rmBEAM}}/2\text{SNR}$ . We also note that the noise level increases where there is a nearby strong maser source in the same channel. This is because the data have a limited dynamic range of about 900 in the presence of strong sources.

## 2.2 Calibration

To edit and calibrate the data, we used CASA (version 4.1.0)<sup>1</sup> with a modified VLA pipeline 1 (version 1.2.0)<sup>2</sup>. The

pipeline does automatic flagging for eg. zeros or shadowing of antennas. Additional flagging for Radio Frequency Interference (RFI) and bad antennas was done manually. The pipeline also applies the bandpass, flux and complex gain calibrations to the data. We do not use Hanning smoothing and do not recalculate the data weights at the end of the pipeline. We subsequently perform further flagging and editing by hand. More details on the calibration of the pilot study are also given in Bihl et al. (2015). A full description of our quality check method will be presented in our forthcoming overview paper (Beuther et al., *in preparation*).

## 3 MASER IDENTIFICATION

Maser sites were identified in a similar fashion as the methods described in Walsh et al. (2012). We initially used the DUCHAMP software (Whiting 2015) package to identify maser candidates. The data cubes contain pixels ( $5''$ ) that are approximately four times smaller than the FWHM size of the restoring beam ( $20''$ ) and the channel width is  $0.73 \text{ km s}^{-1}$ . Based on these specifications for the data cubes, we used DUCHAMP to search for emission at twice the rms noise level, which is typically 19mJy/beam, in the full cubes, with the following minimum thresholds for detection: no less than 12 pixels in a single channel, no less than 25 voxels and no less than 2 consecutive channels over which the emission was above the  $2\sigma$  level. This effectively constrains a detection to occur at above the  $2\sigma$  level in each of as many pixels would fill half a beam for each of two consecutive channels in the cube. By varying these input parameters and comparing the results, we found this to be the best compromise to maximise the number of real detections made, whilst simultaneously limiting the number of false detections. We also found that, within reasonable limits, the number of real and false detections did not change greatly when varying the input parameters slightly. This gives us confidence that our input parameters are reasonably robust.

During our initial DUCHAMP searches, it became clear that such automated source finding was limited by the changing noise levels in the data. In particular, the edges of the survey area had higher noise levels in all channels, but also, the limited dynamic range (approximately up to 900) close to very strong masers significantly increases the noise, in the images containing strong emission. The effect on DUCHAMP results was that many more false detections would be made. In order to mitigate the effects of changing noise levels, a noise map was created for each data cube, based on averaging data over a velocity range where no masers were expected ( $-110$  to  $-70 \text{ km s}^{-1}$ ). This full data cube was divided by the noise map, effectively creating a signal-to-noise cube, which was then searched for sources in DUCHAMP.

Figure 1 shows a peak flux density map for the 1612 MHz data cube (top) and a signal-noise peak flux density map (bottom). The top map shows increased noise levels at the edges, as well as sidelobe patterns from the strongest masers, with the strongest located at G31.102-0.219. The signal-to-noise map shows improve-

<sup>1</sup> <http://casa.nrao.edu/>

<sup>2</sup> <https://science.nrao.edu/facilities/vla/data-processing/pipeline>

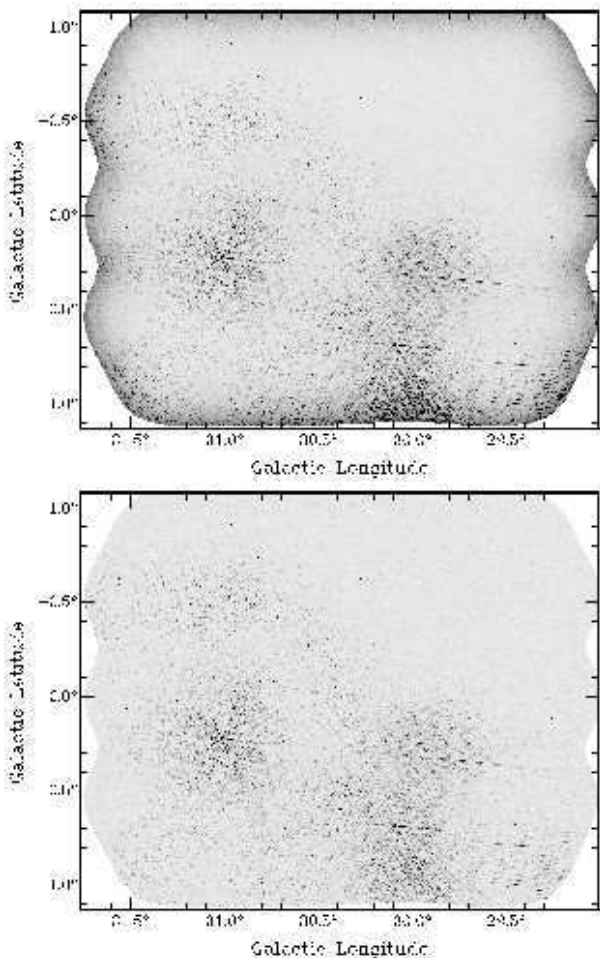


**Figure 1.** The upper panel shows the peak temperature map for the 1612 MHz data (as an example). Bright masers can be seen as unresolved dark points. However, the map is dominated by noisy regions that are associated with the brightest masers and interference. The edges of the map also show increased noise levels. The lower panel shows a signal to noise map where the effects of noise at the edge of the map have been greatly reduced. The effects of bright masers and interference have also been reduced, but not to such a great extent. In the full data cube, the effects of bright masers and interference only manifest in a small number of channels, which can be individually flagged.

ment, particularly along the edges of the survey area. However, the sidelobes from strong masers remain. These maser sidelobes occur in only one or two channels of the data cube. We find that within a primary beam (about  $0.25^\circ$ ) of a strong maser, any other potential masers are hidden within the sidelobes. However, this is only the case for one or two channels that are strongly affected. At other channels, we are able to search for potential masers that are close (in the plane of the sky) to a strong maser, but at a different velocity.

In order to confirm detections by DUCHAMP as real masers, we visually inspected each DUCHAMP detection. Nearly all false detections can be identified as sidelobes from nearby strong masers. In addition to identifying masers through confirmation of DUCHAMP detections, we

also visually inspected the data cubes and moment maps, using the HOPSfind method of which more details can be found in Walsh et al. (2012). This method was particularly successful for the 1612 MHz data cube as 1612 MHz masers, when associated with evolved stars, often display a characteristic double-horned profile in their spectra (signifying an expanding shell containing the masing gas), which is easy to identify by eye, even at low signal-to-noise levels.

For each identified maser spot, we use the MIRIAD task “imfit” to fit the emission and derive positions and relative uncertainties, as well as peak flux densities. We derive the velocity minima and maxima for maser spots by visually inspecting the data cubes and determining over which channels emission is seen.

### 3.1 Discussion of Completeness

The completeness limit of the VLA observations will vary depending on the noise level. In a region of the data that overlaps in velocity with a bright maser and is spatially close to the maser, the sidelobe noise level will be high and the completeness will have a correspondingly low value. Given that OH masers associated with star formation are likely to be clustered within the same star formation site, it is also likely that the number of masers will be slightly underestimated because these high noise regions surrounding bright masers will contain a higher density of masers. Therefore, it is not possible to accurately compute a single completeness level, but it makes more sense to compute completeness levels as a function of changing noise levels.

The noise levels at which 10, 50, 90 and 95 per cent of the data are below this level are 11, 19, 22 and 27 mJy/beam per  $0.73 \text{ km s}^{-1}$  channel, respectively. We use these noise levels as representative of the data and apply these noise levels to a Monte Carlo simulation. In the simulation, we take representative data with noise at each of these levels and artificially inject point sources into the noisy data. The point sources have a line width typical of masers:  $2 \text{ km s}^{-1}$ . We then use our same source-finding methods described above and count the number of recovered point sources. We can then plot four distributions of the completeness levels, as shown in Figure 2.

The completeness distributions show that nearly all data is complete at around the level of 0.25 Jy/beam, but that 50 per cent of the data is complete at around the level of 0.17 Jy/beam.

## 4 RESULTS

The detected masers are detailed in Table 1 and their positions and spectra are shown in Figure 3. We find a total of 276 maser spots (128 at 1612 MHz, 72 at 1665 MHz, 72 at 1667 MHz, and 4 at 1720 MHz). The brightest maser spot has a peak flux density of 124.7 Jy and the weakest 19 mJy.

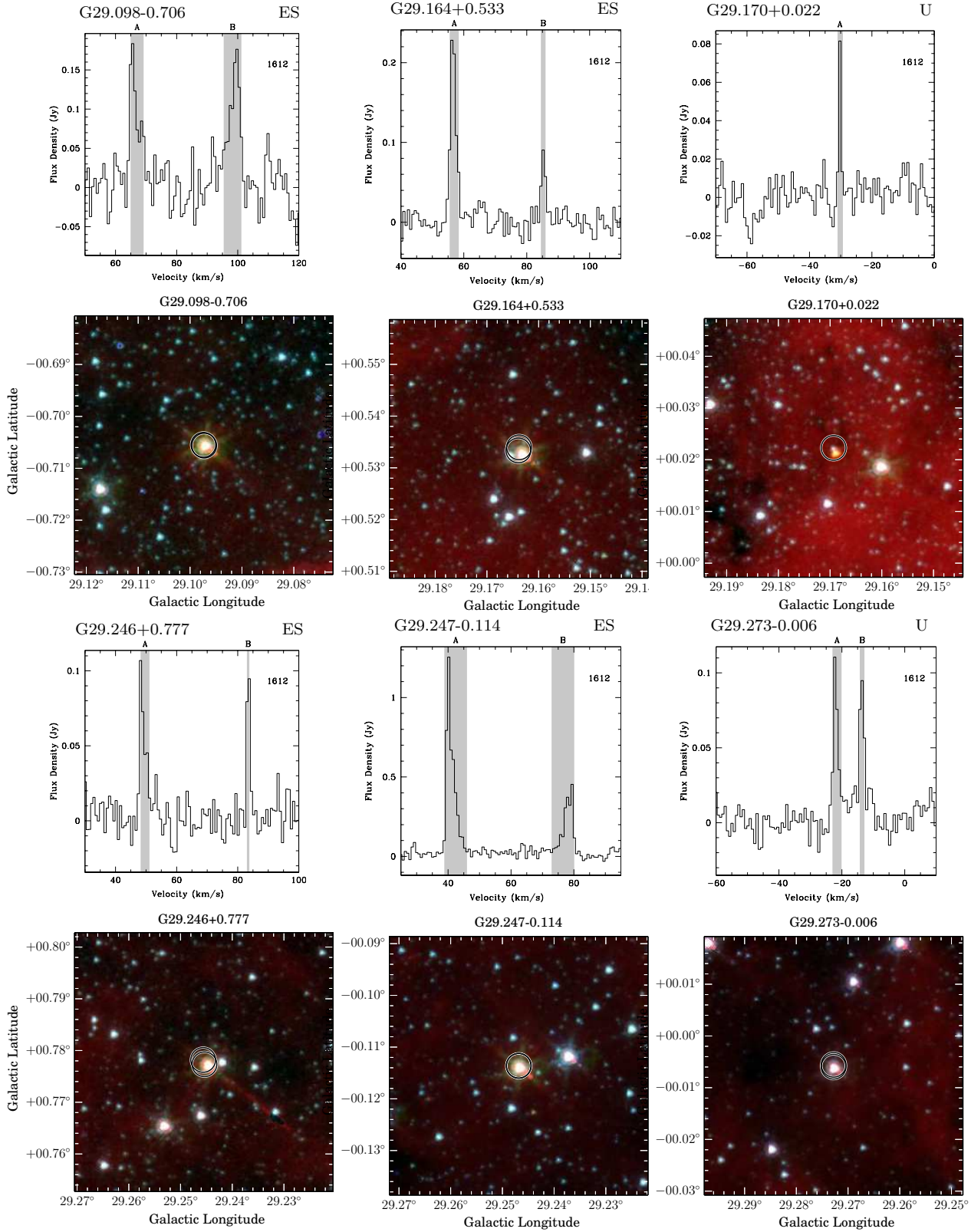


**Figure 3.** The environments of detected masers. The upper panel shows the spectrum of OH emission with the horizontal axis showing  $V_{\text{LSR}}$  in  $\text{km s}^{-1}$  and the vertical axis showing flux in Janskys integrated over the source. Shaded areas indicate the velocity range over which emission is detected for each maser spot. GLIMPSE 3-colour images are shown: blue =  $3.5 \mu\text{m}$ , green =  $4.5 \mu\text{m}$  and red =  $8.0 \mu\text{m}$ . Symbols represent the positions of maser spots. 1612 MHz masers are shown as circles, 1665 MHz masers as squares, 1667 MHz masers as diamonds and 1720 MHz masers as triangles. The axes are in Galactic coordinates. Designations for each maser site are shown in the upper-right corner, where ES = evolved star, SF = star formation and U = unknown origin. Note that the size of the symbols does not represent the relative or absolute position uncertainties of the masers. The full Figure can be found online.

**Table 1.** Details for maser spots detected in this work. The first column lists the name assigned to each spot, which is based on the Galactic coordinates and the OH transition which shows the emission. Columns 2 to 7 give the position of the maser spot. Column 8 lists the peak flux density, based on the strongest channel. Column 9 lists the rms noise level, determined from the spectrum. Column 10 lists the integrated flux. Columns 11, 12 and 13 list the peak velocity of maser emission and the minimum and maximum velocities over which emission is detected, respectively. The relative uncertainty in the position is given in columns 14 and 15. Note that the absolute position uncertainty is about  $2''$ . The last column lists comments on each maser site. The full table can be found online.

Name	RA		Dec		Flux			Velocity ( $\text{km s}^{-1}$ )			Position		Comments <sup>1</sup>
	(J2000) ( $^{\text{h}}\text{m}^{\text{s}}$ )	(J2000) ( $^{\circ}\text{'}$ )	(J2000) ( $^{\circ}\text{'}$ )	(J2000) ( $^{\circ}\text{'}$ )	Peak (Jy)	rms (mJy)	Integrated ( $\text{Jy.km s}^{-1}$ )	Peak	Min.	Max.	Uncertainty ( $''$ ) Lon.	Lat.	
G29.098-0.706-1612A	18 46 57.108	-03 44 02.97	0.18	30	0.54	66.6	64.9	69.2	2.1	2.3	ES - D,BS		
G29.098-0.706-1612B	18 46 57.122	-03 44 03.72	0.18	30	0.65	98.8	95.4	101.2	2.2	2.3			
G29.164+0.533-1612A	18 42 39.431	-03 06 33.22	0.228	13	0.509	56.8	55.5	58.4	0.99	0.99	ES - D,BS		
G29.164+0.533-1612B	18 42 39.289	-03 06 32.65	0.090	13	0.140	85.4	84.5	86.0	2.6	2.5			
G29.170+0.022-1612A	18 44 29.300	-03 20 16.73	0.079	9	0.081	-30.2	-31.0	-29.5	3.5	3.8	U - RS		

<sup>1</sup>Masers are associated with evolved stars (ES), star formation (SF), or unknown (U). D means that the 1612 MHz spectrum shows a double-peaked feature between 14 and 47  $\text{km s}^{-1}$  wide, which is associated with evolved stars. BS, RS and wkS mean that in the GLIMPSE images, a Bright, Red or weak Star is seen co-spatial with the maser site, respectively. nPL means near a pulsar. IRDC means the GLIMPSE image shows an infrared dark cloud co-spatial with the maser site and so the maser site is associated with star formation. Where the literature reports a previous observation, a reference is given to identify the association for the maser site: Bel13 – Beltrán et al. (2013), Blo94 – Blommaert, van Langevelde & Michiels (1994), Cas95 – Caswell et al. (1995), Cod10 – Codella et al. (2010), Dea07 – Deacon et al. (2007), Deg04 – Deguchi et al. (2004), DiF08 – Di Francesco et al. (2008), Fel02 – Felli et al. (2002), He05 – He et al. (2005), Hil05 – Hill et al. (2005), Ima13 – Imai et al. (2013), Kwo97 – Kwok, Volk & Bidelman (1997), Kur94 – Kurtz, Churchwell & Wood (1994), Lou93 – Loup et al. (1993), Mot03 – Motte, Schilke & Lis (2003), Per09 – Peretto & Fuller (2009), Pes05 – Pestalozzi, Minier & Booth (2005), Ros10 – Rosolowsky et al. (2010), Sev01 – Sevenster et al. (2001), Tho06 – Thompson et al. (2006), Urq09 – Urquhart et al. (2009), Wal98 – Walsh et al. (1998), Win75 – Winnberg et al. (1975).

The maser spots can be grouped into maser sites. Maser sites occur at well defined positions on the sky (usually smaller than  $1''$  and very small compared to our beam size; Forster & Caswell 2000) and may consist of maser spots from multiple transitions. We identify a total of 103 maser sites. Figure 4 shows a Venn diagram of the number of maser sites that exhibit emission in the four masing transitions. We find that approximately half (53 per cent) of the maser sites contain only the 1612 MHz transition and approximately 10 per cent of the maser sites fall into each of the following categories: sites with 1612+1665+1667 MHz emission, 1665+1667 MHz emission and with 1665 MHz emission only. The remaining categories are typically sparsely populated. We note that the relative number of detections in all categories is consistent with results from SPLASH (Dawson et al. 2014) who have performed a pilot untargetted survey of ground-state OH masers in the Southern Hemisphere.

We show the spectra and infrared environments of each maser site in Figure 3. For each maser site, the upper panel shows the spectrum or spectra, where maser emission was detected. The shaded regions in each spectrum indicate the range of velocities over which maser emission was detected and the top of each spectrum shows a letter to label maser spots. Note that the shaded areas were determined by inspection of the full data cube and include channels only where emission could easily be identified at a single location. Thus, there are secondary peaks that lie outside the shaded regions. In such cases, we have determined that these peaks are either noise spikes or sidelobe emission from nearby (but unrelated) strong maser peaks. Therefore the shaded areas should be used as a guide to identify

the velocity range over which we consider there to be real emission arising from this maser site. The lower panel shows a GLIMPSE 3-colour image (based on 3.5, 4.5 and  $8.0\mu\text{m}$  for blue, green and red colours, respectively) and symbols to represent the positions of the maser spots. The GLIMPSE resolution is between  $1''.7$  and  $2''.0$  and the astrometric accuracy is typically  $0''.3$ .

#### 4.1 Comments on individual sources of interest

*G29.574+0.118.* This maser site contains both 1612 and 1667 MHz masers and appears to be located close to a candidate magnetar (AX 1845.0-0258). The position of the candidate magnetar is offset  $56''$  from the maser site (Olausen & Kaspi 2014). The candidate magnetar is a pulsar with a 7s second period and this pulsar is likely associated with the G29.6+0.1 SNR (Gaensler, Gotthelf & Vasisht 1999). The SNR extends over an area approximately  $5'$  across and the maser site is found within the bounds of the SNR. The GLIMPSE image shows there is an infrared stellar object at the position of the maser site, which does not show a strongly rising flux at longer wavelengths, as might be expected for an evolved star or star forming region. This star may therefore be an unrelated field star. Nothing obvious is seen at the position of the pulsar (G29.564+0.106). There appears to be a filamentary IRDC within an arcminute of the maser site (above the maser site in Figure 3), but does not overlap with the maser site. The maser spectra show emission in both the 1612 and 1667 MHz lines, with the 1667 MHz spectrum showing two unusually broad maser spots, spanning 9.8 and  $18.2\text{km s}^{-1}$ . We have classified this maser site as of

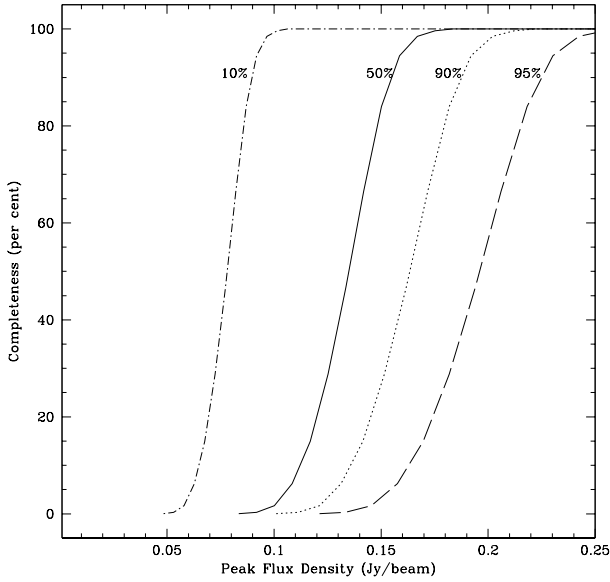


**Figure 2.** Completeness distributions are shown for four representative noise levels. The dot-dash line shows the distribution where 10 per cent of all the data has a better noise level than 11 mJy/beam. The solid line shows the distribution where 50 per cent of all the data has a better noise level than 19 mJy/beam, the dotted line shows the distribution where 90 per cent of all data has a noise level below than 22 mJy/beam and the dashed line shows the distribution where 95 per cent of all data has a noise level below than 27 mJy/beam.

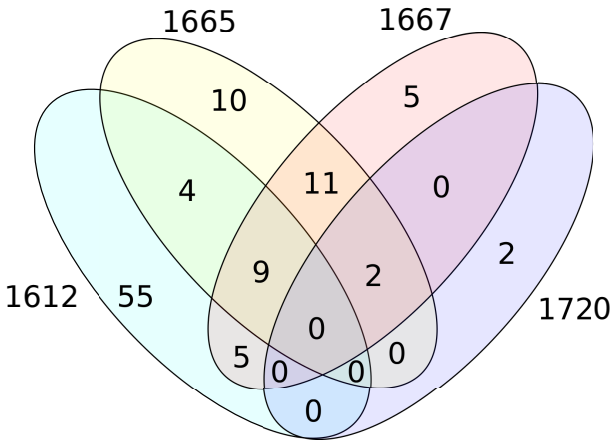


**Figure 4.** A Venn diagram showing the occurrence of maser species for the 103 identified OH maser sites.

unknown association. It is not clear whether or not there is a physical association between the maser site and the candidate magnetar or SNR. If there is an association, it would certainly be interesting to investigate further. One possible method to decide if there is an association or not is to search for periodic variability in the maser signal that matches that of the pulsar. Such periodicity in OH masers has been reported for the 1720 MHz line (Weisberg et al. 2005).

*G31.128-1.015.* This maser site shows emission in the 1667 MHz line. The emission is broken up into four maser spots that together span a velocity range of  $145.3 \text{ km s}^{-1}$ .

The data indicate that emission is present over this entire velocity range. We have assigned this site to unknown origin. The GLIMPSE image shows the maser site is co-spatial with a bright and red star. The Galactic latitude of the site is just over  $1^\circ$ , which indicates that the site is probably close to us, which would favour an evolved star interpretation.

We note that both G30.394-0.706 and G30.944+0.035 exhibit similar characteristics of broad emission in the 1667 MHz line, although the velocity ranges are not as extreme. Both these maser sites also show emission in the 1612 and 1665 MHz lines. The 1612 and 1665 MHz lines are also unusually broad in G30.394-0.706. Both are assigned to an evolved star origin.

## 5 DISCUSSION

### 5.1 The molecular cloud complex W43

The portion of the Galactic plane ( $l=29-32$ ,  $b=\pm 1$ ) considered in this study is host to the molecular cloud complex W43, often referred to as the W43 mini-starburst complex due to its high star formation activity (Motte, Schilke & Lis 2003; Nguyen Luong et al. 2011). Along the line of sight, there is another molecular cloud complex having  $V_{\text{LSR}} \sim 50 \text{ km s}^{-1}$ , with emission seen from  $+35$ – $+55 \text{ km s}^{-1}$ , which is different from  $80$ – $120 \text{ km s}^{-1}$  – the LSR velocity of the W43 complex. Beuther et al. (2012) suggested that these two complexes are interacting due to their location at the end of the Galactic Bar (Nguyen Luong et al. 2011). In Figure 5 we show the  $^{13}\text{CO}$  (1–0) velocity-integrated intensity map and in Figure 6, the latitude-integrated position-velocity (pv) diagram and overlay the positions of the OH maser sites. The maser sites are generally scattered around the integrated map and the pv diagram. However, there are some differences between the maser transitions. 1612 MHz masers are widely scattered within the field of view and within the pv diagram, with no close association with W43 or the feature at a velocity of  $50 \text{ km s}^{-1}$ . This is because 1612 MHz masers are mainly associated with evolved stars and not with the molecular gas.

The four 1720 MHz maser sites, as discussed in Section 5.2.1, are associated with star formation, two of which are within the W43 molecular cloud complex and one associated with the  $50 \text{ km s}^{-1}$  feature (see Figures 5 and 6). The 1665/1667 MHz maser sites seem more closely clustered to the spatial and velocity range of W43 and  $50 \text{ km s}^{-1}$  complexes, especially around the location of W43-Main, where large-scale shocks are strong (Nguyen Luong et al. 2013) and where the molecular gas show double peaks profiles (Beuther et al. 2012). The 1665/1667 MHz masers around W43-Main seem to have a velocity spread within the range  $50$ – $120 \text{ km s}^{-1}$ . This indicates the dynamic nature of this region and may be more evidence of the interaction between the two complexes.



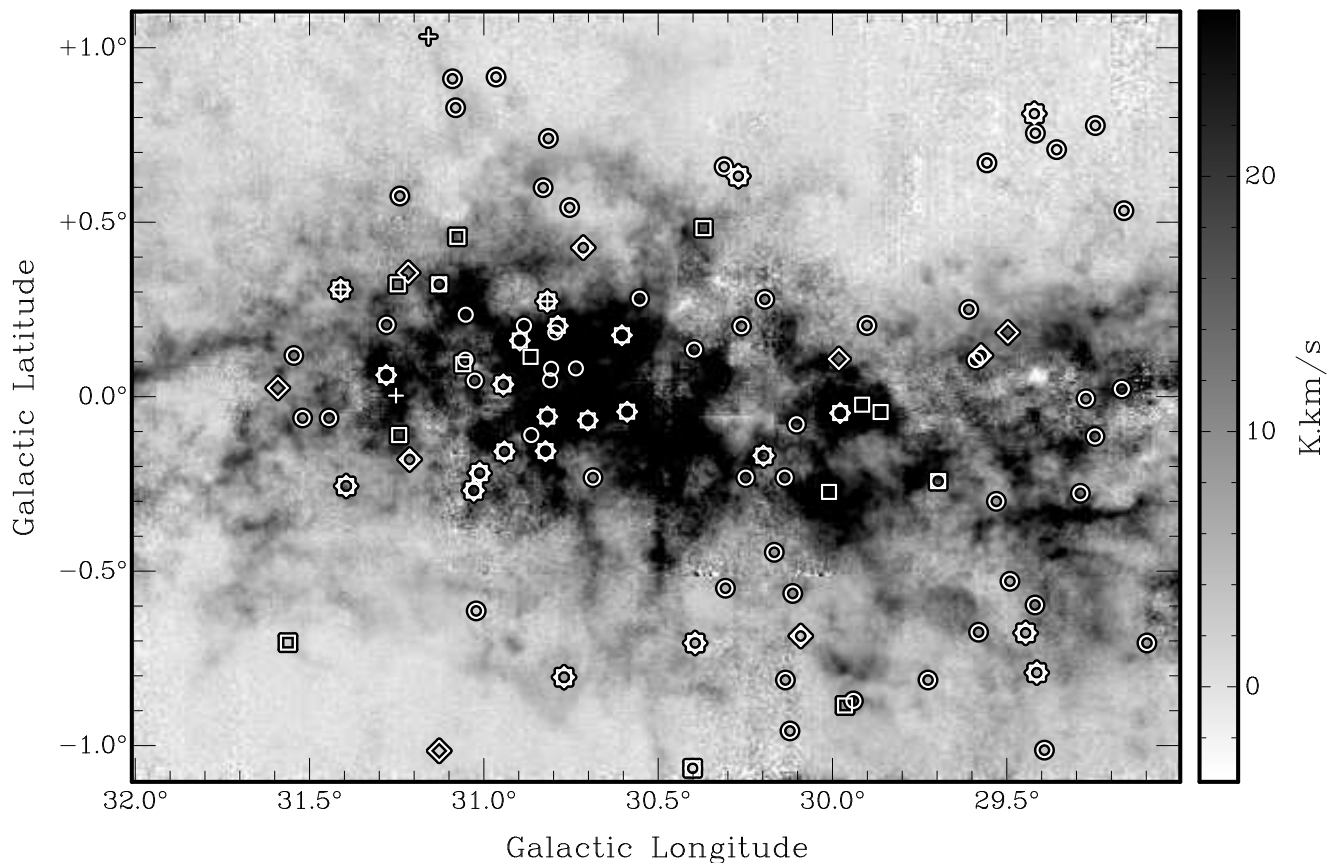


**Figure 5.** The greyscale image shows the distribution of  $^{13}\text{CO}$  (1–0) velocity-integrated gas that includes the W43 complex and a second complex typified by gas at around  $50\text{ km s}^{-1}$ . Maser sites are shown with the following symbols: 1612 - circles; 1665 - squares; 1667 - diamonds ; 1720 - plus signs.

## 5.2 Association of maser sites

Here we use the word “associate” and its derivatives to imply that two objects are (or were) in close enough proximity that the appearance of one object today is considered to be (or have been) significantly affected by the other object. For example, an OH maser may be considered associated with a star formation site in the sense that the star formation site creates the physical conditions conducive to the OH maser (ie. without the star formation site the maser would not exist). Alternately, an OH maser may be considered associated with a star formation site if the star formation site merely increases the available pumping photons for the OH maser (ie. without the star formation site the maser could still exist, but with a significantly reduced intensity).

OH masers are known to be associated with multiple astrophysical objects including evolved stars, star formation and supernova remnants (SNRs). Evolved stars tend to be prominent in the 1612 MHz transition, star formation sites are more prominent in main-line masers (Reid & Moran 1981) and SNRs occasionally show 1720 MHz masers (Wardle & Yusef-Zadeh 2002). However, these transitions are not exclusively associated with these objects. For example, all four transitions are seen as masers towards the same star-forming region (eg. G351.775-0.536

Caswell, Green & Phillips 2013).

In order to associate each maser site in Table 1 with an astrophysical object, we use a search radius of  $20''$  and then search through the literature, using SIMBAD<sup>3</sup>. In the last column of Table 1, we identify associations (where possible) using the literature. If it is not possible to identify associations in this way, then the spectra and GLIMPSE images are used to make an association. If the spectrum shows a double-peaked profile in the 1612 MHz transition, then we assign the maser site to an evolved star origin. Usually, such a maser site is also accompanied by a bright star in the GLIMPSE image. If the GLIMPSE image shows an infrared dark cloud, then the maser site is assigned to a star formation association. However, if the maser site shows both a double-peaked 1612 MHz maser spectrum and is projected in front of an infrared dark cloud, then the association remains unknown. Using this method, we identify 47 maser sites as associated with evolved stars, 30 associated with star formation and 26 with unknown associations.

We caution that Miras (and semi-regular stars with thinner circumstellar envelopes than OH/IR stars, may

<sup>3</sup> <http://simbad.u-strasbg.fr/simbad/>

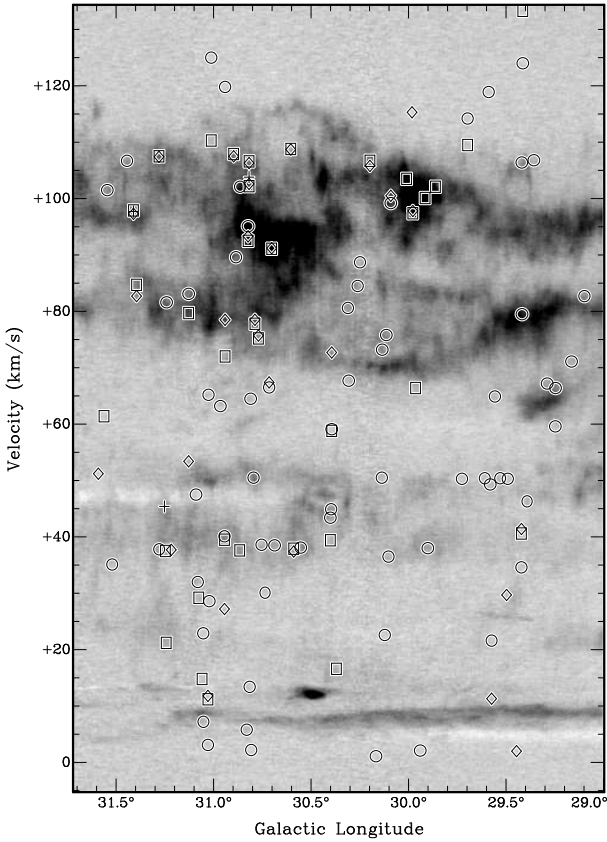


**Figure 6.** Position-velocity diagram using the same  $^{13}\text{CO}$  (1–0) data as Figure 5. Maser sites are shown with the following symbols: 1612 - circles; 1665 - squares; 1667 - diamonds; 1720 - plus signs. The main-line masers (1665/1667) are more closely associated with the concentrations of CO gas than the satellite-line masers (1612/1720), both in position and velocity. The W43 complex is usually located between velocities of  $[+80; +120]\text{km s}^{-1}$ , whereas there is a secondary cloud complex in the velocity range  $[+35; +55]\text{km s}^{-1}$ . Features in the velocity range  $[0; +20]\text{km s}^{-1}$  are most likely foreground clouds along the line of sight.

be devoid of 1612 MHz emission altogether and/or show stronger main line emission (the so called “type I Miras”) with not so well-defined double-peaked profiles in some cases. This is especially true if the classification is based on a single observation, as we have done, as the spectrum can vary with time (Etoka et al. 2001). We expect that some of the unknown associations are indeed evolved stars of this type, since we require a previous evolved star association or a double-peaked profile.

### 5.2.1 1720 MHz maser associations

As mentioned above, sources that are *only* masing on the 1720 MHz transition are normally associated with SNRs, while some high-mass star forming regions with main-line (1665/1667 MHz) masers may also show 1612 and/or 1720 MHz masers (see, eg. Argon, Reid & Menten 2000). We detect four 1720 MHz maser sites in the pilot survey region. Three of these (G30.818+0.273, G31.252+0.003 and

G31.411+0.307) are associated with star formation and the other maser site (G31.159+1.032) is not associated with a known object. More details on these associations are given below:

*G30.818+0.273* is associated with a methanol maser site (Caswell et al. 1995), with the most accurate known position for the methanol maser site (Walsh et al. 1998) offset less than one arcsecond from the 1720 MHz position and overlapping in velocity. This is strong evidence for a star formation association. This maser site also includes main-line masers (1665/1667 MHz) which also supports a star formation association.

*G31.159+1.032* does not appear to be associated with anything in the literature, with no other OH masers detected in any of the other transitions, or any association in the GLIMPSE image and so the origin remains unknown. The 1720 MHz detection is made at an unusually high velocity ( $181.2\text{km s}^{-1}$  – higher than the terminal velocity at this longitude of  $110\text{km s}^{-1}$ ) and is weak ( $0.22\text{Jy}$ , equivalent to a  $5.5\sigma$  detection). This peak is strong enough for us to classify it as a detection in this work, but further observations should be carried out to confirm (or otherwise) this as a bona fide maser site since it is possible that the peak is an unusually high noise spike.

*G31.252+0.003* is co-spatial with a sub-millimetre continuum source (Di Francesco et al. 2008), as well as co-spatial with a red star that appears embedded in a low-contrast IRDC in the GLIMPSE image. In this context, we define “co-spatial” as overlapping in the plane of the sky. Therefore, it is likely associated with star formation. However, we note that only 1720 MHz maser emission is found here. If this is a site of star formation, then it is of a very rare class where 1720 MHz masers are seen, but not the main-line masers.

*G31.411+0.307* is associated with a methanol maser site (Caswell et al. 1995), with the most accurate known position for the methanol maser site (Walsh et al. 1998) offset two arcseconds from the 1720 MHz position and overlapping in velocity. This is strong evidence that this maser site is associated with star formation. This is also supported by the detection of main-line masers at this site.

Three out of four 1720 MHz maser sources are associated with star formation, with only G31.159+1.032 remaining as an unknown association. Two of the star formation maser sites are also associated with main-line masers, while the third (and the unknown association) only shows 1720 MHz masers. Sources that only show maser emission in this single line are almost exclusively associated with SNRs. G31.252+0.003 may be a notable exception to this, as we associate it with star formation, based on the presence of a sub-millimetre continuum source and reddened stellar object, which appears to be embedded in an infrared dark cloud. Another exception is the FU Ori star V 1057 Cyg toward which Lo & Bechis (1974) first detected 1720 MHz (only) OH maser emission. In this violently variable star, as in SNRs, the maser pump may be related to shock excitation.

### 5.2.2 1612 MHz maser associations

We detect 72 sites with 1612 MHz maser emission. Sixty-four per cent (46) are associated with evolved stars, thirteen per cent (9) are associated with star formation and twenty-four per cent (17) are unknown associations. Seventy-six per cent of 1612 MHz maser sites (55) only show emission in the 1612 MHz line. These numbers demonstrate the close association between 1612 MHz maser sites and evolved stars. Further to this, we find that every maser site associated with an evolved star contains 1612 MHz maser emission.

There are five 1612 MHz maser sites that are associated with evolved stars, but do not show any significant emission in the GLIMPSE images (G29.392-1.013, G29.491-0.529, G29.530-0.300, G29.609+0.250 and G30.795+0.184). Indeed, none of these sites show  $\mu$ m emission at 24  $\mu$ m in MIPS GAL (Carey et al. 2009) images either. If these maser sites are indeed associated with evolved stars, then they must have very thick envelopes that have extremely high extinction, rendering the central star undetectable in the GLIMPSE images. Such thick envelopes would imply very high mass-loss rates.

### 5.2.3 1665/1667 MHz maser associations

Out of 11 maser sites that show only 1665 MHz emission, we find that eight of them are associated with star formation, with the rest remaining unknown. In contrast to this, there are five maser sites that show only 1667 MHz emission but all of them have unknown associations. We also find 11 maser sites with both 1665 and 1667 MHz maser emission and all of these are associated with star formation. It is interesting that there are differences in the association rate. In particular that most of the 1665-only masers are associated with star formation, whereas none of the 1667-only masers have known associations. However, we caution that our sample sizes are too small to draw strong conclusions on these differences and await for greater numbers from the full THOR survey to determine if these differences are significant.

Of all the main-line maser sites (ie. any maser site that includes 1665 and/or 1667 MHz masers – forty-six in total), fifty-four per cent (25) are associated with star formation, fifteen per cent (7) are associated with evolved stars and thirty per cent (17) have unknown associations. Thus, our results are in accordance that the main-line maser sites are typically associated with star formation. We also note that in this sample of forty-six main-line maser sites, ninety-six per cent (44) appear to have an infrared counterpart in the GLIMPSE image (ie. bright or red star, IRDC or co-spatial extended emission). Of the two that have no GLIMPSE counterpart, one is a 1665 MHz maser site: G31.247+0.322 and one is a 1667 MHz maser site: G31.217+0.355. This high detection rate of GLIMPSE counterparts is similar to (and possibly slightly higher than) the detection rate of GLIMPSE counterparts to water masers, reported by Walsh et al. (2014): ninety-two per cent. The slightly higher detection rate towards OH masers may be because OH

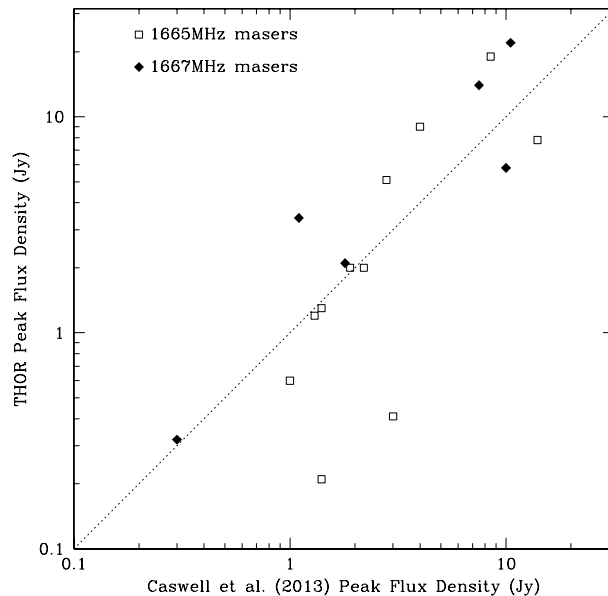


**Figure 7.** Distribution of main-line OH maser peak flux densities, compared between our THOR data and data presented in Caswell, Green & Phillips (2013). 1665 MHz masers are shown as open squares and 1667 MHz masers are shown as filled diamonds. The dotted line shows equality between the two datasets.

masers associated with star formation are present at slightly later stages of evolution than water masers (Breen et al. 2010). At later stages of evolution, we expect that infrared sources will be more easily detectable. However, we again caution that our sample size is too small to draw a strong conclusion.

## 5.3 Comparison with other OH maser surveys

### 5.3.1 Main line masers

Recently, Caswell, Green & Phillips (2013) reported previous and new observations of main-line OH masers, using the Parkes radio telescope. They found twelve OH maser sites within the THOR pilot region, all of which were also detected in our observations. In Figure 7 we show a comparison of the peak flux densities for these masers, by comparing data taken in 2005 to our data – a time difference of approximately 6.5 years. The Figure shows some scatter, but good general agreement between the two datasets. This suggests that whilst there may be some variability in individual objects, these are not large variations of more than a factor of a few. The variations are larger than expected from errors in the flux calibration scales between the different telescopes, since these errors are typically less than 50 per cent for any one measurement. The good general correspondence also shows consistency in the calibration of our data, when compared to that of Caswell, Green & Phillips (2013).

### 5.3.2 1612 MHz masers

In the THOR pilot data we detect 72 1612 MHz OH masers. Sevenster et al. (2001) (hereafter S01) conducted

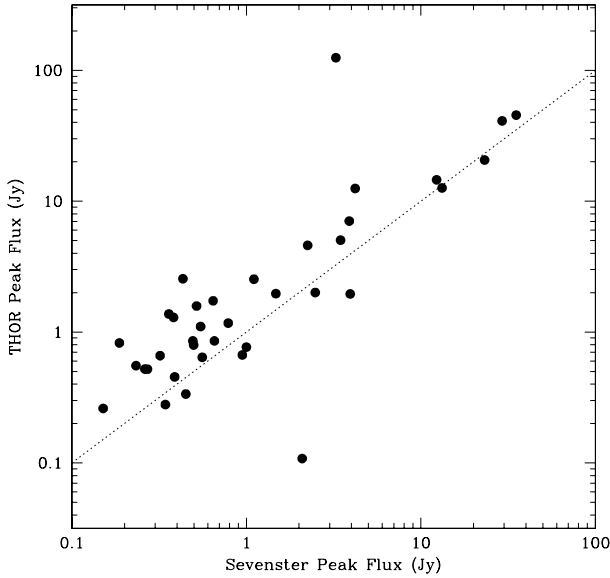


**Figure 8.** Distribution of 1612 MHz OH maser peak flux densities, compared between our THOR data and data from S01. Only maser sites that were detected in both surveys are shown. The dotted line shows equality between the two datasets. Note that we have included one data point for each peak in the spectrum. Since these 1612 MHz OH maser sites all exhibit a double-horned profile, there are 40 data points shown - twice the number of maser sites. The dotted line shows equality between the two datasets.

an untargetted survey of 1612 MHz masers, covering the THOR pilot survey region, but with a number of small holes in their coverage. In the region covered by the THOR pilot survey, S01 detected 21 maser sites, of which all but one are also detected in this work. The one undetected maser in this work is located at G31.091-0.686. We find no evidence for a maser here above a  $3\sigma$  noise level of 48 mJy. We note that the coordinates given by S01 are exactly one degree away from a very strong maser at G30.091-0.686 which was detected by both S01 and us. Also, the shape of the maser spectra, shown by S01 for both maser sites is virtually identical, except for the intensity scale. Finally, inspection of GLIMPSE images show nothing obvious at the position of G31.091-0.686. We therefore suspect that G31.091-0.686 is a spurious detection, although we cannot rule out the possibility that there is a real maser at this position and intrinsic variability has rendered it undetectable during our observations. Thus, we consider 20 maser sites detected by S01 within the THOR pilot area, all of which were also detected in our observations.

In Figure 8, we show the distribution of peak flux densities detected in both surveys. The Figure shows a scatter in the data points, which may be attributed to intrinsic variability, which is rarely larger than a factor of a few. However, nearly all the data points are found above the line of equality, indicating that the THOR peak flux densities are measured consistently higher than those by S01. One maser spot from G30.944+0.035 has a significantly lower flux measured in THOR (0.1 Jy), compared to S01 (2.085 Jy), which makes this data point stand out well below the line in Figure 8. Since the other maser spot in this site shows similar peaks in both datasets, we consider this

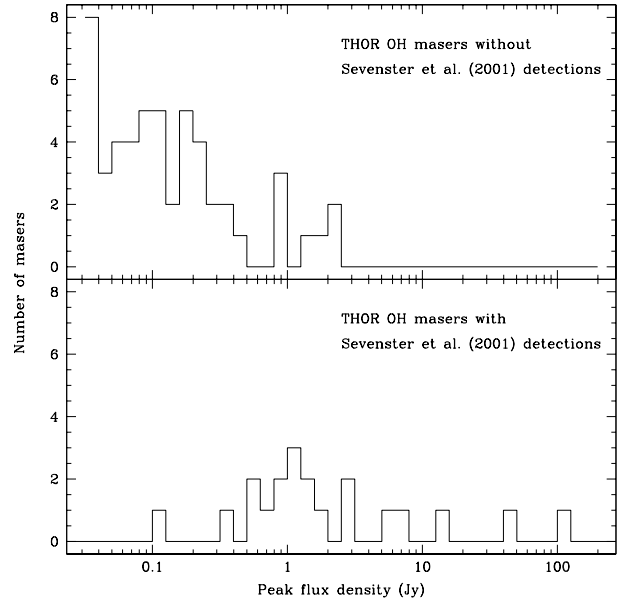


**Figure 9.** Distributions of 1612 MHz OH maser peak flux densities, detected in THOR. The upper distribution shows those OH masers that were not detected by S01 and the lower distribution shows those OH masers that were also detected by S01.

strong evidence for variability in this one maser spot peak. Discounting this one spot, we can calculate the average ratio of THOR to S01 peak flux densities, where we find the S01 peak is 28 per cent of the THOR peak flux.

A similar discrepancy was found between OH maser surveys reported by Dawson et al. (2014). They reported that consistently lower fluxes of OH masers measured by Sevenster et al. (1997) were due to the large channel widths used by Sevenster et al. (1997) which tend to reduce the peak flux densities of narrow maser spots. We believe that the large channel width used by S01 ( $2.27 \text{ km s}^{-1}$ ) provides a similar explanation for the discrepancy in Figure 8. Indeed, S01 estimate that their peak flux densities are about 35 per cent of their true value, due to the wide bins used in their observations.

As mentioned above, in the THOR pilot data we detect 72 1612 MHz OH masers. Therefore, we have detected seventy-one per cent (51) of maser sites that were not found by S01. In Figure 9, we show distributions of the THOR peak fluxes for masers that were and were not found by S01. The S01 99 per cent completeness level is 500 mJy, whereas the THOR completeness level is around 250 mJy a factor of about two times more sensitive than S01. Thus, we expect that many of the peaks only detected in THOR will be weak, rendering them undetectable by S01. This appears to be the case in Figure 9, where most peaks are below 0.3 Jy. But there are also some strong peaks above 1 Jy in the THOR data which were not detected by S01. It is likely that these peaks have undergone intrinsic variability between the observations for the two surveys. Such long term variability has been detected in OH masers and appears to be common (eg. Caswell, Green & Phillips 2013).

#### 5.4 Comparison with dust emission

We have compared the positions of the OH maser sites with dust emission traced by ATLASGAL, which is an unbiased sub-millimetre survey of the inner Galactic plane (Schuller et al. 2009). Matching the masers with the ATLASGAL Compact Source Catalogue (Contreras et al. 2013; Urquhart et al. 2014) we identify 24 OH maser sites that are co-spatial with compact dust emission. Of these, 23 OH maser sites have already been associated with star formation as described in §5.2, including three of the 1720 MHz OH masers associated with star formation. These associations are further strengthened by the good correlation between the velocities of the thermal lines (eq., CO, NH<sub>3</sub>) and the velocities of the peak maser emission (typically better than a few km s<sup>-1</sup> for all associations).

The one OH maser site not previously associated with star formation is G30.823–0.156. This source has been associated with an evolved star, due to the presence of the distinctive double-horned profile seen in the 1612 MHz transition and a bright infrared star seen in the GLIMPSE images that is co-spatial with the maser site. This maser site is one of the most active with a total 12 other 1665 and 1667 MHz OH masers, strong CO and dust emission and extended far-infrared emission seen in Hi-GAL images (Molinari et al. 2010). All of these tracers are normally associated with star forming regions but may also be detected in evolved stars with thick circumstellar envelopes. Further tests are needed to convincingly resolve the nature of this site.

We note that 8 of the sources identified in §5.2 as being associated with star formation are not associated with an ATLASGAL source (G29.446–0.677, G29.915–0.023, G30.249–0.232, G30.307–0.549, G30.311+0.659, G30.397+0.135, G30.941–0.157 and G31.213–0.180). This is somewhat surprising since the dust emission is tracing the distribution of dense gas, which is the raw material for star formation. These maser sites may simply be associated with more distant star formation regions that fall below the detection threshold of the ATLASGAL survey ( $5\sigma \sim 300$  mJy beam<sup>-1</sup>), which corresponds to  $\sim 100 M_{\odot}$  at a distance of 5 kpc.

#### 5.5 Star formation maser sites and continuum emission

The presence of radio continuum emission in sites of star formation is usually a signature of a young HII region (eg. an ultracompact HII region). These regions arise from young high-mass stars, once they have created a sufficient ionising photon flux to dominate the star’s immediate surroundings. Thus, the presence of radio continuum emission indicates a reasonably well developed star forming region. Masers may be seen in earlier stages than the HII regions, although there is some overlap (eg. Forster & Caswell 2000). Recent work (Breen et al. 2010) has suggested that OH masers may appear at a slightly later stage of evolution than other masers, such as water or methanol masers. Evidence for this is the greater prevalence of OH maser sites associated with

radio continuum emission, compared to water or methanol maser sites.

Forster & Caswell (1989) found that 23 out of 74 OH maser sites (31 per cent) were associated with continuum emission. However, their sample was targeted towards known regions of star formation at the time, which may bias the sample to more evolved regions. Our observations remove this bias by covering an untargetted section of the Galactic plane. We can compare continuum emission (Bihl et al. *in preparation*) detected in THOR with the incidence of OH maser sites associated with star formation. There are 31 OH maser sites associated with star formation and of these, 18 are associated with continuum emission (58 per cent). Thus, we find a higher proportion of OH masers associated with continuum sources. We believe this is due to the more sensitive continuum data from THOR, compared to those of Forster & Caswell (1989). But this may suggest that timelines of high-mass star formation may need to be revised to account for a slightly longer OH maser site phase. We caution that this result is based on only a small number of OH maser sites. More robust statistics will be available from the full THOR survey, as well as from SPLASH.

#### 5.6 Diffuse OH emission and absorption

OH can be detected either as masers or as what is sometimes referred to as “thermal” emission or absorption. However, as noted by Dawson et al. (2014), the line profiles often considered thermal may show departures from the permitted LTE line ratios, even in the 1667 and 1665 MHz main lines (see also Crutcher 1979). Similarly, it is very common for the 1612 and 1720 MHz satellite lines to be anomalously excited, with excitation temperatures that are subthermal in one line, and either very high or negative in the other – the latter case being indicative of weak, low-gain maser action. Therefore, rather than referring to such line profiles as thermal emission or absorption, we refer to them as diffuse OH. The typical signature is broad, weak profiles, with all transitions showing similar line widths. In regions where the continuum background is significantly elevated above the CMB, such diffuse OH profiles typically show an almost symmetrical pattern of emission/absorption in the satellite lines, and main lines that are either both in emission or both in absorption (see e.g. Dawson et al. 2014).

During our search of OH masers, we identified 12 sites showing diffuse OH. The details of the strongest emission and absorption features are given in Table 2 and their line profiles and positions are shown in Figure 10. Of the 12 diffuse OH sites, all but three (G30.533+0.021, G30.854+0.151 and G31.388–0.382) show main-line absorption and well-detected satellite line features that are approximate mirror images of each other. The remaining sites also show main-line absorption, but with weak or absent detections in one or both of the satellites.

We note that the intensity ratios of the main-lines vary somewhat, with many showing departures from the 5:9 ratio (1665:1667) expected from an optically thin gas in LTE. This behaviour is expected to arise either from optical

**Table 2.** Diffuse OH sources. Details, following the format of Table 1 are reported for those regions that show spectral profiles indicative of diffuse OH, rather than strong maser emission. Such sources show either inverted profiles in the two satellite lines or lines only in absorption. Details are reported for the strongest OH emission or absorption features. The peak flux density value is based on either the highest (most positive) or lowest (most negative) channel in each spot.

Name	RA	Dec	Peak Flux Density (Jy)	Velocity (km s <sup>-1</sup> )			Position Uncertainty		Comments
	(J2000) (h m s)	(J2000) (° ' ")		Peak	Min.	Max.	Lon. (")	Lat. (")	
G29.937-0.052-1612A	18 46 09.859	-02 41 16.99	0.14±0.03	101.2	99.3	102.4	2.3	2.1	SF - Urq09
G29.937-0.052-1665A	18 46 09.500	-02 41 18.72	-0.19±0.02	102.0	96.8	102.4	2.1	2.0	
G29.937-0.052-1667A	18 46 09.500	-02 41 18.72	-0.23±0.02	102.0	96.8	102.4	2.2	2.2	
G29.937-0.052-1720A	18 46 08.897	-02 41 27.58	-0.10±0.02	102.1	99.3	102.4	5.3	6.1	
G29.956-0.016-1612A	18 46 03.982	-02 39 20.69	0.11±0.03	99.8	100.5	101.9	2	1.9	SF - Tho06
G29.956-0.016-1665A	18 46 03.730	-02 39 22.12	0.21±0.03	98.3	97.8	98.5	1	1	
G29.956-0.016-1665B	18 46 03.750	-02 39 23.04	0.10±0.03	102.0	101.3	103.4	2.4	2.3	
G29.956-0.016-1720A	18 46 04.086	-02 39 25.18	-0.09±0.04	99.8	100.5	101.9	4.1	4.0	
G30.533+0.021-1665A	18 46 59.359	-02 07 23.41	-0.04±0.01	95.0	90.0	95.0	6.3	5.2	SF - Urq09
G30.533+0.021-1667A	18 46 59.116	-02 07 30.53	-0.04±0.01	93.1	90.0	95.0	2.3	2.1	
G30.688-0.071-1612A	18 47 36.222	-02 01 50.90	-0.24±0.03	92.5	89.2	92.5	3.1	3.1	SF - Pes05
G30.688-0.071-1665A	18 47 35.984	-02 01 49.07	-0.14±0.02	95.7	89.2	95.7	3.1	3.1	
G30.688-0.071-1667A	18 47 36.027	-02 01 49.40	-0.23±0.03	95.7	89.2	95.7	3.1	3.1	
G30.688-0.071-1720A	18 47 36.032	-02 01 49.66	0.22±0.06	91.3	89.2	92.5	3.1	3.1	
G30.689-0.043-1612A	18 47 29.965	-02 00 56.24	-0.15±0.02	91.7	85.7	91.9	3.1	3.2	SF - Mot03
G30.689-0.043-1665A	18 47 30.644	-02 00 54.54	-0.25±0.05	92.9	87.1	93.3	4.0	3.8	
G30.689-0.043-1667A	18 47 30.055	-02 00 54.51	-0.22±0.02	94.3	85.7	94.7	3.1	3.1	
G30.689-0.043-1720A	18 47 29.916	-02 00 57.68	0.23±0.06	90.1	87.1	91.9	3.0	3.0	
G30.720-0.083-1612A	18 47 41.742	-02 00 22.39	0.16±0.03	93.3	92.5	93.9	1.3	1.3	SF - Mot03
G30.720-0.083-1612B	18 47 41.733	-02 00 23.62	0.43±0.07	97.1	96.1	98.3	1.1	1.1	
G30.720-0.083-1665A	18 47 41.652	-02 00 22.27	-0.22±0.01	95.7	89.7	96.2	1.3	1.3	
G30.720-0.083-1667A	18 47 41.652	-02 00 22.27	-0.33±0.01	97.1	90.4	97.6	1.1	1.1	
G30.720-0.083-1720A	18 47 41.652	-02 00 22.27	-0.25±0.01	93.9	90.8	93.9	1.1	1.1	
G30.720-0.083-1720B	18 47 41.652	-02 00 22.27	-0.25±0.07	97.1	96.1	98.3	1.1	1.1	
G30.735-0.056-1612A	18 47 37.965	-01 58 55.07	-0.13±0.02	93.2	87.8	93.2	3.1	3.1	SF - Ros10
G30.735-0.056-1665A	18 47 38.242	-01 59 06.62	-0.21±0.02	94.3	89.2	94.8	3.8	3.8	
G30.735-0.056-1667A	18 47 38.613	-01 58 46.99	-0.15±0.01	94.2	89.9	94.8	2.6	2.6	
G30.735-0.056-1720A	18 47 38.607	-01 58 55.94	0.07±0.01	91.5	87.8	93.2	3.6	3.6	
G30.742+0.006-1612A	18 47 25.092	-01 56 45.09	-0.20±0.01	91.8	89.1	91.9	1.6	1.6	SF - Mot03
G30.742+0.006-1665A	18 47 25.585	-01 56 21.90	-0.10±0.02	82.3	81.0	82.8	4.6	4.6	
G30.742+0.006-1665B	18 47 25.457	-01 56 34.41	-0.24±0.02	91.8	89.8	93.3	2.6	2.6	
G30.742+0.006-1667A	18 47 25.451	-01 56 43.35	-0.19±0.01	82.3	81.0	82.8	3.3	3.3	
G30.742+0.006-1667B	18 47 25.329	-01 56 46.91	-0.30±0.01	91.6	89.8	93.8	1.9	1.9	
G30.742+0.006-1720A	18 47 25.261	-01 56 47.37	0.22±0.01	90.6	89.8	91.2	1.6	1.6	
G30.752-0.057-1612A	18 47 39.816	-01 57 57.41	0.75±0.02	96.9	96.1	97.6	1.2	1.2	SF - Cas95
G30.752-0.057-1665A	18 47 38.534	-01 57 47.95	-0.23±0.03	97.8	88.1	98.3	3.2	3.1	
G30.752-0.057-1667A	18 47 38.656	-01 57 44.39	-0.45±0.02	96.4	89.8	96.9	2.3	2.3	
G30.752-0.057-1720A	18 47 39.843	-01 57 53.51	-0.21±0.02	97.3	93.9	97.6	3.2	3.2	
G30.815-0.053-1612A	18 47 44.511	-01 54 35.64	-0.34±0.04	97.6	92.4	97.5	1.1	1.1	SF - Cas95
G30.815-0.053-1665A	18 47 44.986	-01 54 39.29	-0.50±0.03	98.5	92.0	98.5	1.2	1.2	
G30.815-0.053-1667A	18 47 44.748	-01 54 37.47	-0.64±0.03	99.9	92.0	100.0	1.1	1.1	
G30.815-0.053-1720A	18 47 44.870	-01 54 33.91	0.47±0.03	96.3	92.0	100.0	1.1	1.1	
G30.854+0.151-1612A	18 47 06.170	-01 46 41.10	-0.05±0.01	96.7	92.6	96.9	6.3	6.2	SF - Hil05
G30.854+0.151-1665A	18 47 06.280	-01 46 55.43	-0.11±0.01	96.4	92.6	96.9	2.3	2.3	
G30.854+0.151-1667A	18 47 06.523	-01 46 48.32	-0.11±0.01	96.4	92.6	96.9	2.2	2.2	
G31.388-0.382-1665A	18 49 59.141	-01 32 48.11	-0.02±0.01	-3.4	-5.0	-3.0	5.3	5.1	U
G31.388-0.382-1665B	18 49 58.781	-01 32 49.84	-0.02±0.01	18.1	17.2	19.7	2.3	2.1	
G31.388-0.382-1667A	18 49 58.776	-01 32 58.79	-0.05±0.01	-3.3	-6.0	-3.0	4.2	4.2	
G31.388-0.382-1667B	18 49 58.897	-01 32 55.22	-0.10±0.01	18.2	17.2	19.7	2.3	2.2	

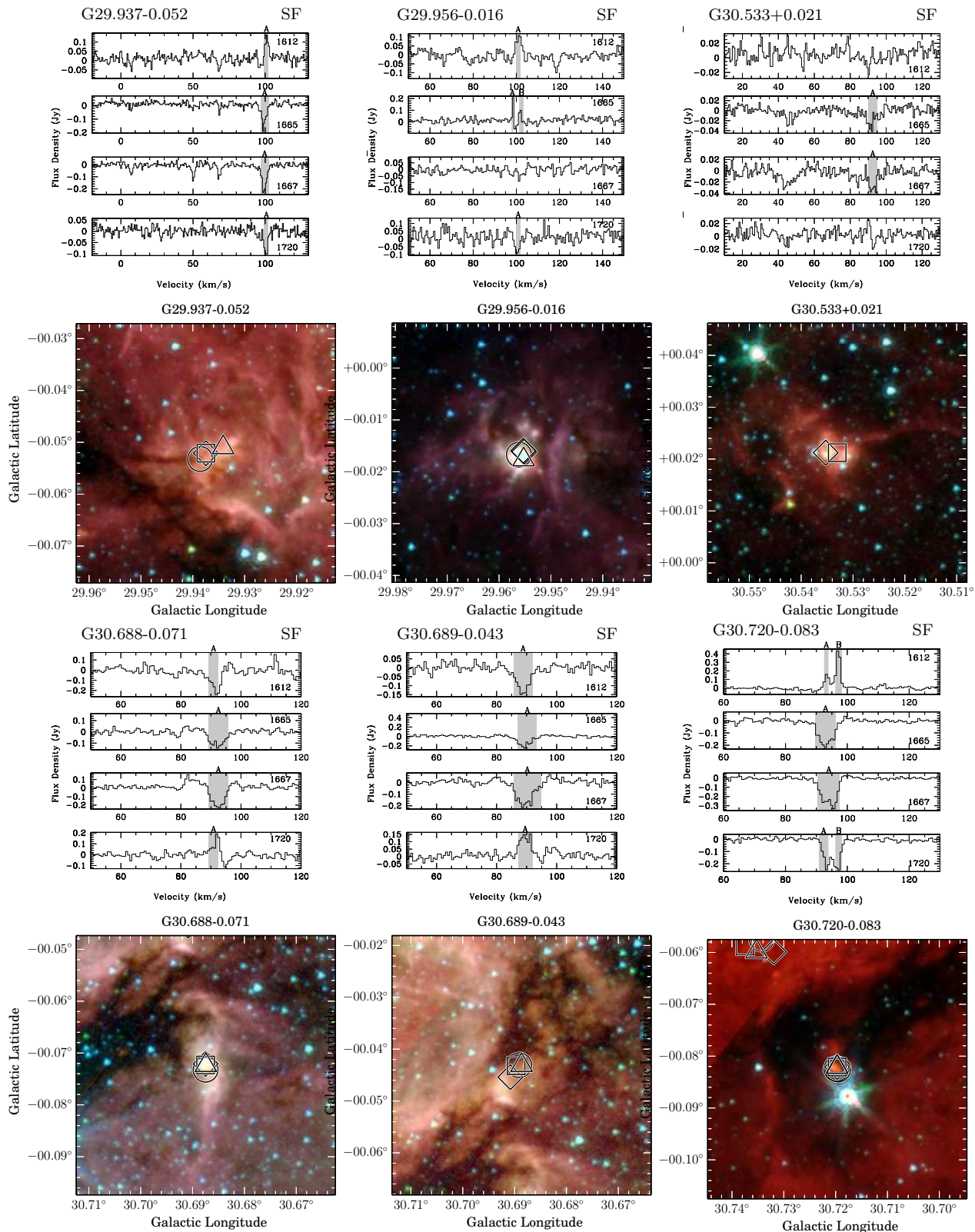


**Figure 10.** Spectra and infrared images for sites of diffuse OH emission and absorption. These sites are identified by the mirror-image 1612 and 1720 MHz OH spectra. GLIMPSE 3-colour images are shown: blue = 3.5  $\mu\text{m}$ , green = 4.5  $\mu\text{m}$  and red = 8.0  $\mu\text{m}$ . Symbols represent the positions of strongest emission or absorption. 1612 MHz is shown as circles, 1665 MHz as squares, 1667 MHz as diamonds and 1720 MHz as triangles. The axes are in Galactic coordinates. Designations for each region are shown in the upper-right corner, where SF = star formation and U = unknown origin. The full Figure is available online.

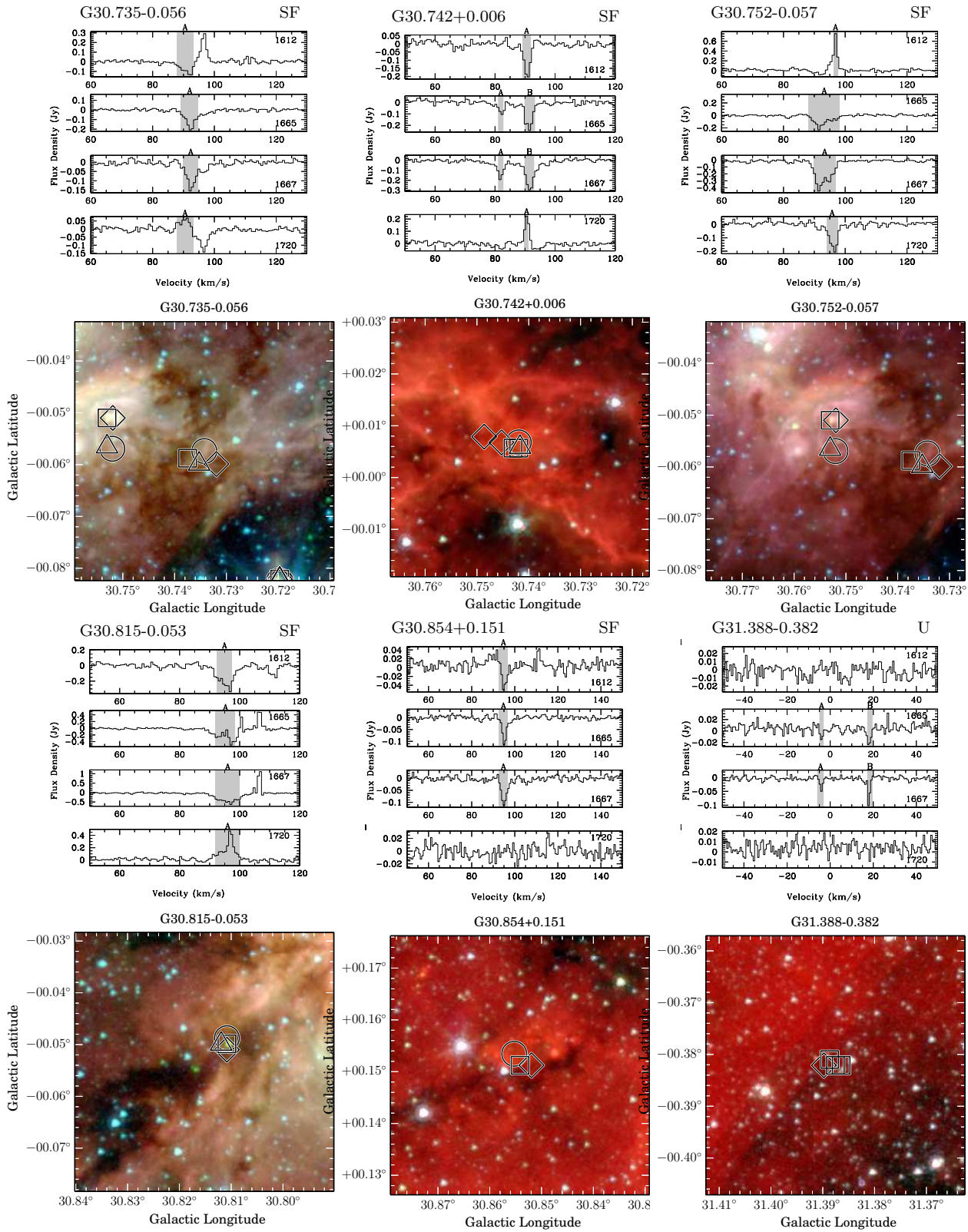


Figure 10 – *continued*



depth effects or from a pattern of excitation temperatures that strongly departs from thermal, with the actual line strengths also set by the difference between these excitation temperatures and the continuum background (see also Dawson et al. 2014).

We also note that some of the spectral features in Figure 10 are likely due to the blending of strong maser emission with diffuse OH features. For example, there are narrow emission features in both the 1665 and 1667 MHz spectra of G30.815-0.053 that do not have any corresponding features in the satellite lines, suggesting that they are the result of high-gain maser action from a localised parcel (or parcels) of gas with strong velocity coherence, and not from the wider diffuse medium.

As shown in Table 2, all but one of the diffuse OH detections are co-spatial with sites of star formation, which may host the molecular gas that gives rise to the diffuse OH, and may also provide the bright continuum background against which the features may be clearly seen. Indeed, most of the diffuse OH is associated with the well known star forming region W43 Main<sup>4</sup> and only the features of G31.388-0.382 are not associated with an established star formation site.

Figure 11 shows the morphology of the 1667 MHz OH absorption in the W43 Main region, in which extended OH absorption is seen against the continuum emission from W43 Main. The Figure shows the maximum optical depth measured at each position. This is calculated from a data cube that contains both the 1667 MHz transition, as well as continuum emission (ie. not continuum subtracted). Maximum optical depth is calculated from the velocity channel that shows the maximum difference between the continuum level (measured at a velocity where there is no OH emission or absorption) and the level at the deepest absorption feature in the spectrum.

We note that the morphology of the optical depth does not match that of the continuum emission. This is expected behaviour because the continuum emission represents the morphology of W43 Main, but the OH that absorbs the continuum originates in a cloud that does not necessarily have the same morphology as the continuum emission. It is not clear if this cloud is an unrelated foreground object, or related to the front envelope of W43 Main. Given that the velocity of the absorption is close to that expected of W43 Main, we consider it more likely that this is part of a foreground envelope.

Most of the region with significant OH absorption shows optical depths around 0.2, indicating that the OH is generally optically thin gas. There are, however, small areas where the optical depth is significantly higher. From this we assume that the OH gas is likely to be optically thin in all but the densest regions, closely linked to star formation

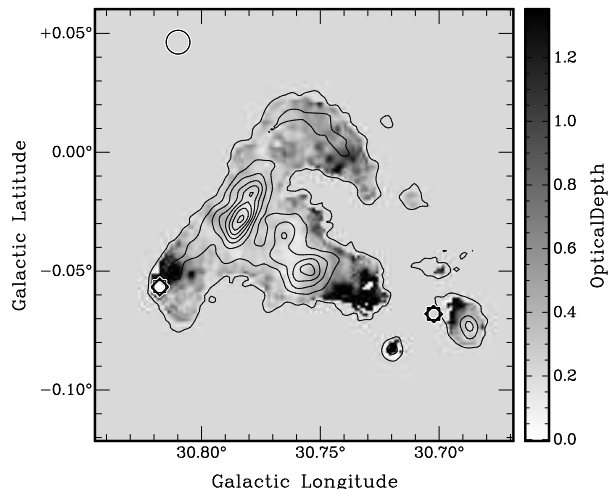


**Figure 11.** Extended OH absorption towards W43 Main. The OH absorption image (shown in greyscale) was created using the 1667 MHz OH data. This map shows the distribution of maximum optical depth at each position. The map is masked to only include areas where the continuum level is above 80 mJy. The contours represent the continuum level, with the lowest contour being 50 mJy and contours increasing by 200 mJy up to a maximum of 1.45 Jy. Three OH masers are found within this region. There is one 1612 MHz maser that appears outside the continuum contours (circle – G30.810+0.047). There are also two maser sites showing both 1665 and 1667 MHz masers (squares and diamonds – G30.702-0.068 and G30.818-0.057) that occur close to the extended absorption.

centres, like W43 Main.

The extended absorption towards W43 Main appears to be the only place in the THOR pilot region where we detect significantly extended OH absorption; the other detections in Table 2 and Figure 10 are all either spatially unresolved or partially resolved regions. It is expected to see only extended OH absorption towards W43 Main because this is the only region within the field of view which shows strong, extended continuum emission and such continuum emission is required in order to see the OH absorption. The optical depth in these unresolved regions again appears to be about 0.2, indicating that optically thin OH is typical.

## 6 CONCLUSIONS

In the THOR pilot region, we have conducted a search for OH emission and absorption. We have adapted a previous simple search method to identify sites of strong emission and successfully applied it to identify maser sites. We found strong maser emission is common throughout the field, with 1612 MHz masers being the most common and 1720 MHz masers being the rarest. In all, we found 103 sites of strong maser emission within the pilot survey region.

By comparing our results with previous OH maser observations, we find that main-line OH masers occasionally show mild variability up to a factor of a few over a period of years. OH masers in the 1612 MHz satellite line also show

<sup>4</sup> W43 Main is a small region of active star formation at the centre of the W43 complex

occasional variability on similar timescales, but we also identify a small number of these maser that show strong variability with order of magnitude changes in intensity over a period of a few years.

We have compared the positions of the maser sites to infrared images, as well as the published literature, in order to understand the origins of the masers. We found that three out of four 1720 MHz maser sites are associated with sites of star formation. There are 72 1612 MHz maser sites, of which 65 per cent are associated with evolved stars and 11 per cent are associated with star formation. There are 42 maser sites with main-line emission (either 1665 or 1667 MHz), of which 50 per cent are associated with star formation and 17 per cent are associated with evolved stars.

The maser site G29.574+0.118 appears to be located close (within the plane of the sky) to a candidate magnetar. However, we are not able to determine if there is a physical link between the maser site and candidate magnetar. We find that the maser emission from G31.128-1.015 is detected over the entirety of a very large velocity range of  $145.3 \text{ km s}^{-1}$ .

We also detect diffuse OH emission and absorption against locations of bright background continuum. Extended OH absorption is seen towards the well known star-forming region W43 Main, while unresolved or partially resolved detections are seen elsewhere. The OH gas generally appears to be optically thin. The diffuse OH line profiles show a characteristic pattern: main lines are seen in absorption whereas the satellite-line profiles are approximate mirror images in emission and absorption.

We look forward to the full THOR survey, which will identify many more OH masers and provide us with more robust statistics on their relative occurrence in star forming regions and evolved stars. The full survey will also identify more sites where we find diffuse OH absorption and/or emission. Combining with the results of SPLASH, such a greatly expanded dataset can be used to directly assess the OH maser population in the Galaxy, as well as help identify a well-defined sequence for high-mass star formation.

## 7 ACKNOWLEDGEMENTS

We would like to thank the anonymous referee for helpful and insightful comments that have greatly improved the quality of this paper. This research has made use of the SIMBAD database, operated at CDS, Strasbourg, France. The National Radio Astronomy Observatory is a facility of the National Science Foundation operated under cooperative agreement by Associated Universities, Inc. RSK acknowledges financial support by the Deutsche Forschungsgemeinschaft (DFG) via the Heidelberg Sonderforschungsbereich SFB 881 The Milky Way System (subprojects B1, B2, and B8) as well as the Schwerpunktprogramm SPP 1573 "Physics of the Interstellar Medium". RSK also thanks for funding from the European Research Council under the European Community's Seventh Framework Pro-

gramme (FP7/2007-2013) via the ERC Advanced Grant STARLIGHT (project number 339177). This research made use of the Duchamp source finder, produced at the Australia Telescope National Facility, CSIRO, by M. Whiting.

## REFERENCES

- Argon, A. L., Reid, M. J., Menten, K. M. 2000, *ApJS*, 129, 159
- Beichman, C.A., Neugebauer, G., Habin, H.J., Clegg, P.E., Chester, T.J., 1988, *Infrared Astronomical Satellite (IRAS) Catalogs and Atlases Explanatory Supplement*
- Beltrán, M. T. et al., 2013, *A&A*, 552, A123
- Benjamin, R. A. et al., 2003, *PASP*, 115, 953
- Beuther, H. et al. 2012, *A&A*, 538A, 11
- Bihl, S. et al. 2015, *A&A*, 580, 112
- Blommaert, J. A. D. L., van Langevelde, H. J., Michiels, W. F. P., 1994, *A&A*, 287, 479
- Blöcker T. 1995, *A&A*, 299, 755
- Breen, S. L., Ellingsen, S. P., Caswell, J. L., Lewis, B. E. 2010, *MNRAS*, 401, 2219
- Burke, B. F. et al. 1970, *ApJL*, 160, 63
- Burton, M.G. et al. 2013, *PASA*, 30, 44
- Carey, S. J. et al., 2009, *PASP*, 121, 76
- Caswell, J.L., Green, J.A., Phillips, C.J. 2013, *MNRAS*, 431, 1180
- Caswell, J. L., Vaile, R. A., Ellingsen, S. P., Whiteoak, J. B., Norris, R. P., 1995, *MNRAS*, 272, 96
- Churchwell, E. et al., 2009, *PASP*, 121, 213
- Codella, C., Cesaroni, R., López-Sepulcre, A., Beltrán, M. T., Furuya, R., Testi, L., 2010, *A&A*, 510, A86
- Contreras, Y. et al. 2013, *A&A*, 549, A45
- Crutcher, R.M. 1979, *ApJ*, 234, 881
- Dame, T.M., Hartmann, D., Thaddeus, P. 2001, *ApJ*, 547, 792
- Dawson, J. R. et al., 2014, *MNRAS*, 439, 1596
- Deacon, R. M., Chapman, J. M., Green, A. J., Sevenster, M. N., 2007, *ApJ*, 658, 1096
- Deguchi, S. et al., 2004, *PASJ*, 56, 765
- Di Francesco, J., Johnstone, D., Kirk, H., MacKenzie, T., Ledwosinska, E., 2008, *ApJS*, 175, 277
- Egan, M. P., Price, S. D., 1996, *AJ*, 112, 2862
- Etoka, S., Blaszkiewicz, L., Szymczak, M., Le Squeren, A. M., 2001, *A&A*, 378, 522
- Felli, M., Testi, L., Schuller, F., Omont, A., 2002, *A&A*, 392, 971
- Fomalont E., 1999, in Taylor G., Carilli C., Perley R., eds, *ASP Conf. Ser.*, Vol. 180, *Synthesis Imaging in Radio Astronomy II*. Astron. Soc. Pac., San Francisco, p. 301
- Forster, J. R., Caswell, J. L. 2000, *ApJ*, 530, 371
- Forster, J. R., Caswell, J. L. 1989, *A&A*, 213, 339
- Gaensler, B. M., Gotthelf, E. V., Vasisht, G., 1999, *ApJL*, 526, 37
- Ginsburg, A., et al., 2013, *ApJS*, 208, 14
- Green, J. A. et al., 2009, *MNRAS*, 392, 783
- Gwinn, C. R. 1994, *ApJ*, 429, 241
- Haverkorn, M., Gaensler, B. M., McClure-Griffiths, N. M., Dickey, J. M., Green, A. J. 2006, *ApJS*, 167, 230
- He, J. H., Szczerba, R., Chen, P. S., Sobolev, A. M., 2005, *A&A*, 434, 201
- Hill, T., Burton, M. G., Minier, V., Thompson, M. A.,

- Walsh, A. J., Hunt-Cunningham, M., Garay, G., 2005, MNRAS, 363, 405
- Imai, H., Deguchi, S., Nakashima, J.-I., Kwok, S., Diamond, P. J., 2013, ApJ, 773, 182
- Imai, H., Obara, K., Diamond, P. J., Omodaka, T., Sasao, T., 2002, Nature, 417, 829
- Imai, H., Kameya, O., Sasao, T., Miyoshi, M., Deguchi, S., Horiuchi, S. 2000, ApJ, 538, 751
- Jackson, J.M., et al. 2006, ApJS, 163, 145
- Johnston, K. J. et al. 1971, ApJL, 166, 21
- Jordan, C. H., Walsh, A. J., Lowe, V., Lo, N., Purcell, C. R., Voronkov, M. A., Longmore, S. N., 2013, MNRAS, 429, 469
- Kwok, S., Volk, K., Bidelman, W. P., 1997, ApJS, 112, 557
- Kurtz, S., Churchwell, E., Wood, D. O. S., 1994, ApJS, 91, 659
- Lawrence, A. et al., 2007, MNRAS, 379, 1599
- Litvak, M. M. 1971, ApJ, 170, 71
- Lo, K. Y., Bechis, K. P. 1974, ApJL, 190, 125
- Loup, C., Forveille, T., Omont, A., Paul, J. F., 1993, A&AS, 99, 291
- Moran, J. M., Burke, B. F., Barrett, A. H., Rogers, A. E. E., Ball, J. A., Carter, J. C., Cudaback, D. D. 1968, ApJL, 152, 97
- Nguyen Luong, Q. et al. 2013, ApJ, 775, 88
- Nguyen Luong, Q. et al. 2011, A&A, 529A, 41
- Mac Low, M.-M., Klessen, R. S., 2004, Rev. Mod. Phys., 76, 125
- McClure-Griffiths, N. M., Dickey, John M., Gaensler, B. M., Green, A. J., Haverkorn, Marijke, Strasser, S. 2005, ApJS, 158, 178
- McKee, C. F., Ostriker, E. C., 2007, ARA&A, 45, 565
- Molinari, S. et al., 2010, PASP, 122, 314
- Motte, F., Schilke, P., Lis, D. C., 2003, ApJ, 582, 277
- Olausen, S. A., Kaspi, V. M., 2014, ApJS, 212, 6
- Peretto, N., Fuller, G. A., 2009, A&A, 505, 405
- Pestalozzi, M. R., Minier, V., Booth, R. S., 2005, A&A, 432, 737
- Purcell, C. R. et al., 2013, ApJS, 205, 1
- Rathborne, J. M., Jackson, J. M., Simon, R., 2006, ApJ, 641, 389
- Reid, M. J., Moran, J. M., 1981, ARA&A, 19, 231
- Rosolowsky, E. et al., 2010, ApJS, 188, 123
- Sahai, R., Trauger, J. T., 1998, AJ, 116, 1357
- Schuller, F. et al., 2009, A&A, 504, 415.
- Sevenster, M. N., van Langevelde, H. J., Moody, R. A., Chapman, J. M., Habing, H. J., Killeen, N. E. B., 2001, A&A, 366, 481 (S01)
- Sevenster M.N., Chapman J.M., Habing H.J., Killeen N.E.B., Lindqvist M. 1997, A&AS, 124, 509
- Skrutskie, M. F. et al., 2006, AJ, 131, 1163
- Stil, J. M. et al., 2006, AJ, 132, 1158
- Taylor, A. R. et al., 2003, AJ, 125, 3145
- Thompson, M. A., Hatchell, J., Walsh, A. J., MacDonald, G. H., Millar, T. J., 2006, A&A, 453, 1003
- Urquhart, J. S. et al. 2014, A&A, 568, A41
- Urquhart, J. S. et al., 2009, A&A, 501, 539
- Uscanga, L., Gómez, J. F., Suárez, O., Miranda, L. F., 2012, A&A, 547, A40
- Walsh, A. J., Purcell, C. R., Longmore, S. N., Breen, S. L., Green, J. A., Harvey-Smith, L., Jordan, C. H., Macpherson, C., 2014, MNRAS, 442, 2240
- Walsh, A. J., Purcell, C., Longmore, S., Jordan, C. H., Lowe, V., 2012, PASA, 29, 262
- Walsh, A. J., Bertoldi, F., Burton, M. G., Nikola, T., 2001, MNRAS, 326, 36
- Walsh, A. J., Burton, M. G., Hyland, A. R., Robinson, G., 1998, MNRAS, 301, 640
- Wardle, M., Yusef-Zadeh, F., 2002, Science, 296, 2350
- Weisberg, J. M., Johnston, S., Koribalski, B., Stanimirovic, S., 2005, Science, 309, 106
- Whiting, M. T. 2012, MNRAS, 421, 3242
- Winnberg, A., Nguyen-Quang-Rieu, Johansson, L. E. B., Goss, W. M., 1975, A&A, 38, 145
- Wood, D. O. S., Churchwell, E., 1989, ApJS, 69, 831
- Zijlstra, A. A. et al. 2001, MNRAS, 322, 280
- Zinnecker, H., Yorke, H. W., 2007, ARA&A, 45, 481